Plasma Physics and Controlled Fusion

PAPER

Nonlinear response of vertical paired structure in complex plasma

To cite this article: Zhiyue Ding *et al* 2019 *Plasma Phys. Control. Fusion* **61** 055004

View the article online for updates and enhancements.

IOP ebooks™

Bringing you innovative digital publishing with leading voices to create your essential collection of books in STEM research.

Start exploring the collection - download the first chapter of every title for free.

This content was downloaded from IP address 129.62.70.181 on 29/03/2019 at 19:22

IOP Publishing Plasma Physics and Controlled Fusion
Plasma Phys. Control. Fusion **61** (2019) 055004 (13pp) https://doi.org/10.1088/1361-6587/ab062c

Nonlinear response of vertical paired structure in complex plasma

Zhiyue Ding, Ke Qiao, Jie Kong, Lorin S Matthews and Truell W Hyde[1]

Center for Astrophysics, Space Physics and Engineering Research, Baylor University, United States of America

E-mail: Zhiyue_Ding@baylor.edu, Ke_Qiao@baylor.edu and Truell_Hyde@baylor.edu

Received 5 September 2018, revised 23 December 2018
Accepted for publication 11 February 2019
Published 21 March 2019

Abstract

The effect of the ion wake downstream of grains immersed in a flowing plasma is observed experimentally through the apparent non-reciprocal grain–grain interactions. Here we extend amplitude-frequency response analysis to examine the nonlinear components of the interaction of a dust particle pair aligned with the ion flow. The particle pair is modeled as two forced coupled oscillators, and a new coordinate system is introduced in which the breathing and sloshing modes are linearly decoupled. Multiple-scale analysis is used to derive analytical expressions for the response in the vertical direction for each mode in this coordinate system. By fitting the analytical expressions to experimentally measured response curves, the nonlinear part of the wake-modified particle–particle interaction is determined and identified as the source for the coupling between the sloshing and breathing modes. It is found that the restoring force acting on the downstream particle is more linear, thus stabilizing the oscillations of the downstream grain.

Keywords: complex plasma, ion wake, nonlinearity, non-reciprocal grain–grain interaction

(Some figures may appear in colour only in the online journal)

1. Introduction

In a rf discharge plasma, dust particles levitated in the plasma sheath region are greatly influenced by the ion wake which is caused by the streaming ions scattered by the negatively charged dust [1]. For dust particles aligned with the ion flow, the ion wake field downstream of the dust particles lead to an asymmetric interaction potential between the grains [2–11]. Thus the ion wake plays an essential role in the dynamics of small grains in the plasma environment.

Numerical models of the ion wake including particle-in-cell simulations [12–18], Monte Carlo simulation [3, 19–21], or a combination of the two methods [22, 23], generally focus on the dynamics of the electrons and ions. These models have demonstrated that the wake potential behind dust grains takes an oscillating form which facilitates the alignment of dust particles below the upstream grains [15–17, 21]. From the molecular dynamic point of view, the drag force from scattered ions stabilizes this alignment [19]. The charge of the downstream dust grains is also found to be decreased due to the wakefield [14, 18]. Due to the large differences in the characteristic timescales for the electrons, ions and dust, it is computationally challenging to directly model the dynamics of all three species at the same time. MD Simulations on direct modeling the dynamics of dust particles have also been conducted in various manners, including treating the dust as 'dressed' particles with the plasma appearing implicitly through the plasma dielectric function [24–26], modeling the ion wakefield as a point charge at a fixed point downstream of the dust [27], modeling the electrons and ions through fluid equations [28].

In experiment, it is possible to examine the ion wake in terms of the dynamics of the affected dust particles. A paired dust particle structure provides a suitable configuration to examine the ion wake as it is the simplest 1D structure that can be formed which still involves all relevant coupling interaction [6, 29]. Experiments have confirmed the ion-wake-induced decharging effect [5, 30], and shown the instability triggered by the particle–particle interaction under the influence of ion wake [29, 31–35]. Using a linear

[1] Author to whom any correspondence should be addressed.

 © 2019 IOP Publishing Ltd Printed in the UK

approximation of the interaction force, Kong *et al* [36, 37] showed that the particle charge and effective Debye length could be measured by investigating the coupled oscillation of vertical dust pairs inside a glass box. Goree *et al* [38, 39] employed velocity distribution correlations to anlyze the oscillatory modes of dust particle pairs, which allowed them to examine the heating effect caused by the ion wake.

These previous experiments approximated the non-reciprocal particle–particle interaction by assuming a linear interaction potential. To better understand how the ion wake modifies the particle–particle interaction, it is necessary to extend the theory to the nonlinear regime. Nonlinear response analysis are so far limited to the dynamics of a single dust particle [40–42]. Ivlev *et al* [40] studied the nonlinear amplitude-frequency response for a single dust particle in order to test the anharmonic potential in the sheath of a low-pressure rf discharge. Zafiu *et al* [41] related the nonlinear response of a single particle to the position dependent charge variation as well as the asymmetric sheath potential. Wang *et al* [42] showed the effects that other sources can have on the nonlinear response of a single dust particle employing a technique numerically based on a model with self-consistently determined sheath field and dust charge. Shukla *et al* [43, 44] presented a mechanism for self excited large amplitude nonlinear oscillations at very low discharge pressure and studied the response of a dust grain attributing the parametric resonance to the plasma density oscillation by studying the response curves.

Here, we extend the nonlinear-amplitude frequency response analysis to a strongly coupled system with two degrees of freedom for the first time in dusty plasma, and apply amplitude-frequency response to measure the nonlinear contributions of the ion wake to the particle–particle interaction force by studying the coupled motion of a dust particle pair structure aligned with the ion flow and confined within a glass box. Rather than considering the anharmonic sheath potential [40, 41], we instead take the particle–particle interaction as the main source of nonlinearity. We derive the analytical form of particles' motion governed by the nonlinear equations of motion using the multiple scale method, and compare with the experimentally measured response curves to determine the quadratic terms for both the upstream and downstream interaction forces.

2. Theory

A confined, vertically paired dust particle structure under sinusoidal excitation of small amplitude and frequency Ω in a plasma discharge can be modeled as two forced coupled oscillators as shown in figure 1. At equilibrium, dust particles are confined in a parabolic potential well due to the electric field in the plasma sheath region (this assumption of parabolic potential well will be justified later in the discussion section). The variation of the particle–particle interaction force due to the deviation of the inter-particle spacing is attributed to the first and second order terms in the Taylor expansion of the interaction force at the equilibrium inter-particle spacing R_0, where the nonlinearity is introduced by the second order term.

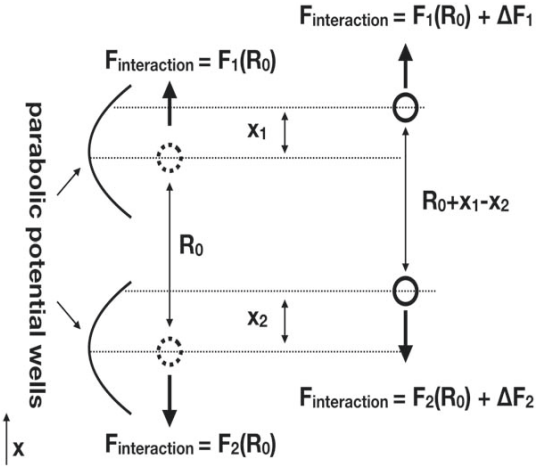

Figure 1. Scheme of the model for a vertically aligned dust particle pair in the plasma sheath region. The dust particles are trapped in parabolic potential wells $\Phi = \frac{1}{2}m_{1(2)}\omega_{1(2)}^2 x^2$. The subscripts 1 and 2 are corresponding to the upstream and downstream dust particle. The varation of the particle–particle interaction force due to the deviation from the equilibrium position is determined by $\Delta F_{1(2)} = -m_{1(2)}[k_{1(2)}(x_{1(2)} - x_{2(1)}) + k'_{1(2)}(x_{1(2)} - x_{2(1)})^2]$, where $k_{1(2)}$ and $k'_{1(2)}$ are related to the first and second derivative of the interaction force at the equilibrium inter-particle distance R_0 through $k_{1(2)} = F'_{1(2)}(R_0)/m_{1(2)}$ and $k'_{1(2)} = F_{1(2)}''(R_0)/2m_{1(2)}$. Here, the interaction force is not presumed to be in any particular form.

By considering neutral gas drag and assuming an identical mass m for both dust particles, the equations of motion in the vertical direction are

$$\begin{aligned}
&\ddot{x}_1 + \mu\dot{x}_1 + \omega_1^2 x_1 + k_1(x_1 - x_2) \\
&\quad + k_1'(x_1 - x_2)^2 \\
&= F_1\exp(\mathrm{i}\Omega t) + \text{c.c.}, \\
&\ddot{x}_2 + \mu\dot{x}_2 + \omega_2^2 x_2 + k_2(x_2 - x_1) \\
&\quad + k_2'(x_2 - x_1)^2 \\
&= F_2\exp(\mathrm{i}\Omega t) + \text{c.c.},
\end{aligned} \tag{1}$$

where x_1 and x_2 are the displacements from equilibrium (1 and 2 being the indices for the upstream and downstream particles), μ is the neutral gas drag coefficient, ω_1 and ω_2 are the frequencies of the vertical confinements provided by the sheath electric field, k_1 and k_2 are the coefficients of the linear interaction between the particles, k_1' and k_2' are the coefficients of the second order terms in the Taylor expansion of the particle–particle interaction forces, F_1 and F_2 (should be distinguished from the interaction force in figure 1) are amplitudes of the external driving in acceleration unit. Here ' c.c.' stands for the complex conjugate (for conciseness, 'c.c.' will be dropped from the following derivations, while all solutions are understood to be accompanied by their complex conjugate components). In most cases, k_1 is not equal to k_2 for two particles aligned in a direction parallel to the ion flow, due to the non-reciprocal ion wake.

To solve these coupled nonlinear equations, we first eliminate the linear coupling terms in x_1 and x_2 by introducing a new coordinate system: $x_+ = x_1 - (\alpha_-)x_2$ and $x_- = x_1 - (\alpha_+)x_2$. Here α_+ (α_-) are the oscillation amplitude ratios for particles 1 and 2 corresponding to the breathing (sloshing) mode, which can be measured experimentally employing the scanning mode spectra (SMS) [45] technique (i.e. an extension of the traditional mode spectra technique where the motion of the two particles is projected onto all the possible eigenvectors). The original equations of motion can now be written in the decoupled form

$$\begin{aligned}\ddot{x}_+ + \mu\dot{x}_+ + \omega_+^2 x_+ + g_1(c_1x_+ - c_2x_-)^2 &= f_+\exp(\mathrm{i}\Omega t)\\ \ddot{x}_- + \mu\dot{x}_- + \omega_-^2 x_- + g_2(c_1x_+ - c_2x_-)^2 &= f_-\exp(\mathrm{i}\Omega t).\end{aligned} \tag{2}$$

In equation (2) g_1, g_2, c_1, c_2 and f_+, f_- are related to the original parameters k_1', k_2', F_1 and F_2 through the relationships:

$$\begin{aligned} g_1 &= (k_1' - \alpha_- k_2')/(\alpha_+ - \alpha_-)^2,\\ g_2 &= (k_1' - \alpha_+ k_2')/(\alpha_+ - \alpha_-)^2, \end{aligned} \tag{3a}$$

$$\begin{aligned} c_1 &= \alpha_+ - 1,\\ c_2 &= \alpha_- - 1, \end{aligned} \tag{3b}$$

$$\begin{aligned} f_+ &= F_1 - \alpha_- F_2,\\ f_- &= F_1 - \alpha_+ F_2. \end{aligned} \tag{3c}$$

In the linear limit, equation (2) provides the equations of motion for the two oscillation modes, i.e. the breathing and sloshing mode, respectively. Their natural frequencies ω_+ and ω_- are directly measured by the SMS technique. In the rest of this paper, we will call x_+ (x_-) the breathing (sloshing) coordinate, α_+, α_- the decoupling parameters, and ω_+ and ω_- the frequencies of the breathing and sloshing modes.

The nonlinear equations in equation (2) can be solved using multiple scale perturbation theory by expanding a test solution across different time scales [46]. In this case, we assume an approximate solution keeping only terms to the order of $o(\epsilon^2)$ as:

$$\begin{aligned} x_+ &= \epsilon x_{+1}(t, t_1) + \epsilon^2 x_{+2}(t, t_1),\\ x_- &= \epsilon x_{-1}(t, t_1) + \epsilon^2 x_{-2}(t, t_1), \end{aligned} \tag{4}$$

where ϵ is a small dimensionless parameter that is used to indicate the order of approximation, x_{+1} and x_{-1} are approximate solutions to first order in ϵ, x_{+2} and x_{-2} are approximate solutions to second order in ϵ^2, and $t_1 = \epsilon t$ is the fast scale time. (See the appendix A for the full derivation of equations (4)–(9).) Inserting these test solutions into equation (2) and equating terms at different orders of ϵ, the equations can now be solved independently for four different regions in terms of the driving frequency Ω: primary breathing (sloshing) regions where Ω is close to the breathing (sloshing) mode frequency $\omega_+(\omega_-)$ and super-harmonic breathing (sloshing) regions where Ω is close to half the breathing (sloshing) frequency $\omega_+(\omega_-)$.

In the primary breathing region, $\Omega = \omega_+ + \delta\epsilon$, where δ is the deviation of the driving frequency Ω from the breathing mode frequency ω_+. The equations of motion to first order take the form:

$$\begin{aligned} \frac{\partial^2 x_{+1}}{\partial t^2} + \omega_+^2 x_{+1} &= 0,\\ \frac{\partial^2 x_{-1}}{\partial t^2} + \omega_-^2 x_{-1} &= f_-\exp(\mathrm{i}\Omega t), \end{aligned} \tag{5}$$

with the solution:

$$\begin{aligned} x_{+1} &= A\exp(\mathrm{i}\Omega t),\\ x_{-1} &= B\exp(\mathrm{i}\Omega t) + \frac{f_-}{-\Omega^2 + \omega_-^2}\exp(\mathrm{i}\Omega t), \end{aligned} \tag{6}$$

while the equations of motion in second order (ϵ^2) take the form:

$$\begin{aligned} \frac{\partial^2 x_{+2}}{\partial t^2} + \omega_+^2 x_{+2} &= -2\frac{\partial^2 x_{+1}}{\partial t\partial t_1}\\ &\quad - \mu\frac{\partial x_{+1}}{\partial t} - g_1(c_1x_{+1} - c_2x_{-1})^2 + f_+\exp(\mathrm{i}\Omega t),\\ \frac{\partial^2 x_{-2}}{\partial t^2} + \omega_-^2 x_{-2} &= -2\frac{\partial^2 x_{-1}}{\partial t\partial t_1}\\ &\quad - \mu\frac{\partial x_{-1}}{\partial t} - g_2(c_1x_{+1} - c_2x_{-1})^2. \end{aligned} \tag{7}$$

It is well known that linear undamped theory predicts unbounded oscillations when Ω is equal to ω_+, irrespective of the excitation amplitude. However, in an actual experimental system these oscillations are generally finite, limited by damping and nonlinearities within the system. Thus, to obtain an uniformly valid approximate solution it is necessary to consider the excitation term (when at resonance) to the same order of ϵ used for the damping and all other nonlinearities [46]. In this case, at breathing resonance the excitation term in the breathing coordinate $f_+\exp(\mathrm{i}\Omega t)$ appears in the equation of motion to second order in ϵ (equation (7)) where both damping and nonlinearity come into effect, while the excitation term in the sloshing coordinate $f_-\exp(\mathrm{i}\Omega t)$ appears in the equation of motion to first order in ϵ (equation (6)). Substituting the first order solution shown in equation (6) into the second order equations of motion given in equation (7) and eliminating the secular terms, A and B are found to be given by

$$\begin{aligned} A &= \frac{f_+}{\mathrm{i}\omega_+(\mu + \mathrm{i}2\delta\epsilon)}\exp(\mathrm{i}\delta t_1) + C\exp\left(-\frac{\mu t_1}{2}\right),\\ B &= C'\exp\left(-\frac{\mu t_1}{2}\right), \end{aligned} \tag{8}$$

where C and C' are constants determined by initial conditions. In this entire derivation, the situation of internal resonance $\omega_+ \approx 2\omega_-$ is avoided, i.e. the possibility of the breathing mode being excited directly by the sloshing resonance is theoretically prohibited.

Substituting equations (8) into (6), the solutions for the primary breathing region yield:

$$x_{+1} = \frac{-f_+}{\omega_+[\mu^2 + 4(\Omega - \omega_+)^2]^{\frac{1}{2}}} \times \exp\left(\mathrm{i}\left[\Omega t + \mathrm{arctg}\left(\frac{\mu}{2(\Omega - \omega_+)}\right)\right]\right) + C\exp\left(-\frac{\mu t_1}{2} + \mathrm{i}\omega_+ t\right), \quad (9a)$$

$$x_{-1} = \frac{f_-}{-\Omega^2 + \omega_-^2}\exp(\mathrm{i}\Omega t) + C'\exp\left(-\frac{\mu t_1}{2} + \mathrm{i}\omega_- t\right). \quad (9b)$$

Following the same procedure, the solutions for the primary sloshing region to first order of approximation take the form:

$$x_{+1} = \frac{f_+}{-\Omega^2 + \omega_+^2}\exp(\mathrm{i}\Omega t) + C\exp\left(-\frac{\mu t_1}{2} + \mathrm{i}\omega_+ t\right), \quad (10a)$$

$$x_{-1} = \frac{-f_-}{\omega_-[\mu^2 + 4(\Omega - \omega_-)^2]^{\frac{1}{2}}} \times \exp\left(\mathrm{i}\left[\Omega t + \mathrm{arctg}\left(\frac{\mu}{2(\Omega - \omega_-)}\right)\right]\right) + C'\exp\left(-\frac{\mu t_1}{2} + \mathrm{i}\omega_- t\right). \quad (10b)$$

The relationship of the primary breathing response x_{+1} to the driving frequency is given by the first term in equation (9*a*), while the primary sloshing response x_{-1} is given by the first term in equation (10*b*). The second term in each of these equations is a transient response corresponding to the natural frequencies of each mode. As can be seen, to first order of approximation, the primary responses are independent of the nonlinear parameters g_1 and g_2. Therefore at a presumed low excitation amplitude (i.e. where only quadratic nonlinearity is considered) the primary response behavior is linear.

In the super-harmonic breathing (sloshing) regions, since there is no primary resonance (i.e. Ω is not close to either ω_+ or ω_-), all excitations need only be considered to first order of ϵ, i.e. all excitation terms should appear only to first order in the equations of motion. Following the same procedure as before, we find the solution for the secondary breathing region to be:

$$x_{+1} = -\frac{g_1\left[c_1\left(\frac{f_+}{-\Omega^2+\omega_+^2}\right) - c_2\left(\frac{f_-}{-\Omega^2+\omega_-^2}\right)\right]^2}{\omega_+[\mu^2 + 4(2\Omega - \omega_+)^2]^{\frac{1}{2}}} \times \exp\left(\mathrm{i}\left[2\Omega t + \mathrm{arctg}\left(\frac{\mu}{2(2\Omega - \omega_+)}\right)\right]\right) + \frac{f_+}{-\Omega^2 + \omega_+^2}\exp(\mathrm{i}\Omega t) + C\exp\left(-\frac{\mu t_1}{2} + \mathrm{i}\omega_+ t\right), \quad (11a)$$

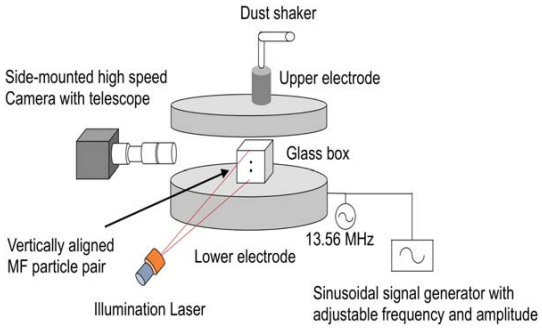

Figure 2. Scheme of the modified GEC RF reference cell with a glass box placed between the upper and lower electrodes employed in this research.

$$x_{-1} = \frac{f_-}{-\Omega^2 + \omega_-^2}\exp(\mathrm{i}\Omega t) + C'\exp\left(-\frac{\mu t_1}{2} + \mathrm{i}\omega_- t\right), \quad (11b)$$

while for the secondary sloshing region:

$$x_{+1} = \frac{f_+}{-\Omega^2 + \omega_+^2}\exp(\mathrm{i}\Omega t) + C\exp\left(-\frac{\mu t_1}{2} + \mathrm{i}\omega_+ t\right), \quad (12a)$$

$$x_{-1} = -\frac{g_2\left[c_1\left(\frac{f_+}{-\Omega^2+\omega_+^2}\right) - c_2\left(\frac{f_-}{-\Omega^2+\omega_-^2}\right)\right]^2}{\omega_-[\mu^2 + 4(2\Omega - \omega_-)^2]^{\frac{1}{2}}} \times \exp\left(\mathrm{i}\left[2\Omega t + \mathrm{arctg}\left(\frac{\mu}{2(2\Omega - \omega_-)}\right)\right]\right) + \frac{f_-}{-\Omega^2 + \omega_-^2}\exp(\mathrm{i}\Omega t) + C'\exp\left(-\frac{\mu t_1}{2} + \mathrm{i}\omega_- t\right). \quad (12b)$$

The secondary responses corresponding to twice the excitation frequencies 2Ω can be clearly seen in equations (11*a*) and (12*b*) as the first terms in x_{+1} (equation (11*a*)) and x_{-1} (equation (12*b*)). In contrast to the primary responses, secondary responses are governed by the nonlinear parameters g_1 and g_2. Therefore, a secondary response with shifted phase can be considered as a direct consequence of the nonlinear particle–particle interaction.

3. Experiment

The experiment discussed here was conducted in a modified gaseous electronics conference RF reference cell shown in figure 2. The lower electrode was powered at 13.56 MHz while the upper electrode was grounded. A 20 mm × 18 mm × 18 mm (height × length × width) glass box was placed on the lower electrode in order to provide the horizontal confinement required to form vertical chain structures. Melamine Formaldehyde particles with diameter of 8.89 ± 0.09 μm were dropped into the plasma through a shaker mounted above the upper electrode, and levitated inside the glass box. Initially, a long chain structure inside the box was

formed at a plasma power of 1.96 W. By carefully reducing the plasma power, dust particles were dropped to the bottom electrode until only two were left in the box. Once a paired structure was formed, the plasma power was increased to its experimental value, 9.82 W, where the small inter-particle distance results in a strongly coupled pair structure.

A function generator coupled to the lower electrode through an 20 dB attenuator was employed to provide a sinusoidal driving force to the particle pair. During the experiment, the driving frequency of the lower electrode was increased from 1 to 50 Hz in steps of 0.1 Hz under a constant driving amplitude of 1 V. The trajectories of the vertically aligned particles at each step were recorded from the side using a high speed CCD camera at 500 frames per second to collect a total of 5000 frames. Throughout the experiment, the gas pressure was held at 40 mTorr, ensuring detection of particle thermal motion, while the plasma power was maintained at 9.82 W.

3.1. Mode decoupling in the sloshing and breathing coordinate

Since the particle pair is driven vertically, all the analysis here is based on the particles' vertical motion. Typically the analysis is done using the coordinate of the center of mass and positions relative to the center of mass. The motion of the center of mass is commonly related to the sloshing mode of the particle oscillation, while the relative coordinate is related to the breathing mode. However, fast Fourier transformation (FFT) of the time series of particles' thermal center of mass motion and relative motion, figures 3(a) and (c) show that there is considerable response at the sloshing frequency for the relative coordinate, and considerable response at the breathing frequency for the center of mass coordinate. The non-reciprocal property of the particle–particle interaction (i.e. $k_1 \neq k_2$) causes the center of mass mode basis set to no longer be orthogonal to the relative mode basis set. It is reasonable to observe both sloshing and breathing components in the center of mass and the relative coordinates, since they characterize the 'pure' sloshing mode (i.e. where the particles are oscillating in phase with the same amplitude of motion) and the 'pure' breathing mode (i.e. where the particles are oscillating 180° out of phase with the same amplitude of motion), respectively.

To separate the different modes in the linear regime for dust particles with nonreciprocal interaction, it is necessary to apply the sloshing and breathing coordinates introduced in section 2. Figure 4 shows the SMS obtained from the particle thermal motion [45]. The mode frequencies ω_+, ω_- and decoupling parameters α_+ and α_- (i.e. the oscillation amplitude ratio) for the two modes were directly measured from the maxima in the SMS at the higher (ω_+) and lower (ω_-) frequencies. The oscillation amplitude ratios $\alpha_+(=-0.35)$ and $\alpha_-(=0.81)$ can now be used to transform the recorded time series of trajectories $x_1(t)$ and $x_2(t)$ for the upstream and downstream particles into decoupled coordinates $x_+(t) = x_1(t) - (\alpha_-)x_2(t)$ and $x_-(t) = x_1(t) - (\alpha_+)x_2(t)$. The FFTs of the particles' thermal motion in the sloshing and breathing coordinates are shown in figures 3(b) and (d), where the the undesired component (i.e. the breathing component in the sloshing coordinate and the sloshing component in the breathing coordinate) is elimated from each mode. It is important to note that the frequency appearing around 30 Hz is due to intrinsic system noise and should be distinguished from the breathing component observed at approximately 32 Hz. From the experimentally measured values of ω_+, ω_-, α_+ and α_-, the linear coefficients and vertical

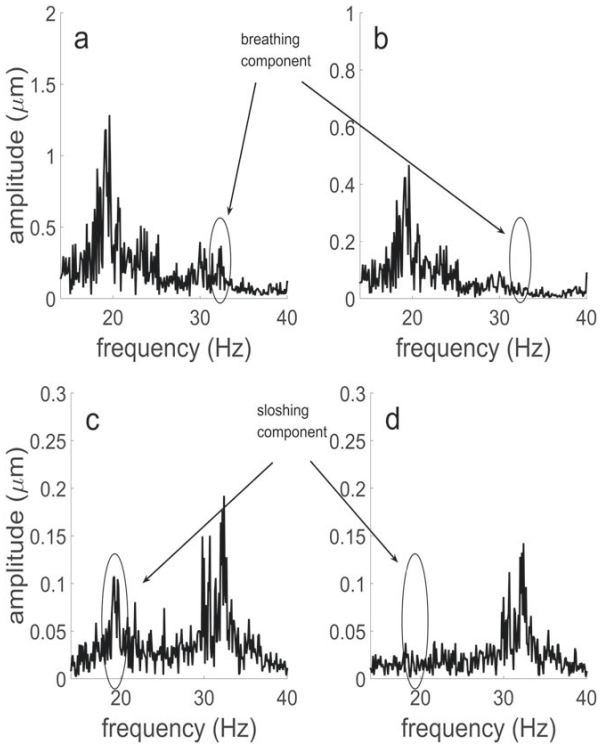

Figure 3. Fast Fourier transform (FFT) of the thermal motion of a particle pair for (a) the conventional center of mass coordinate $(x_1 + x_2)$, (b) the sloshing coordinate $(x_1 - \alpha_+ x_2)$, (c) the relative coordinate $(x_1 - x_2)$ and (d) the breathing coordinate $(x_1 - \alpha_- x_2)$.

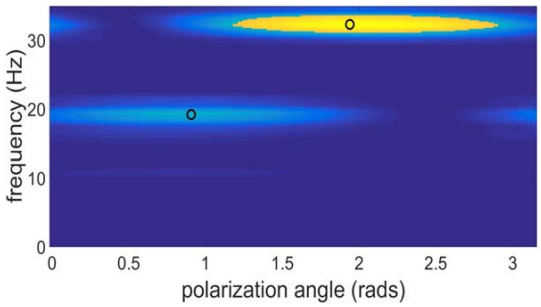

Figure 4. Scanning mode spectra for the particles' thermal motion. The sloshing mode frequency ω_- is approximately 18.5 Hz with polarization $\phi_- = 0.89$ [45]. The breathing mode frequency ω_+ is approximately 32 Hz with polarization $\phi_+ = 1.91$. Decoupling parameters can be determined by taking the cotangent of the polarizations, $\alpha_- = \cot(\phi_-)$ and $\alpha_+ = \cot(\phi_+)$.

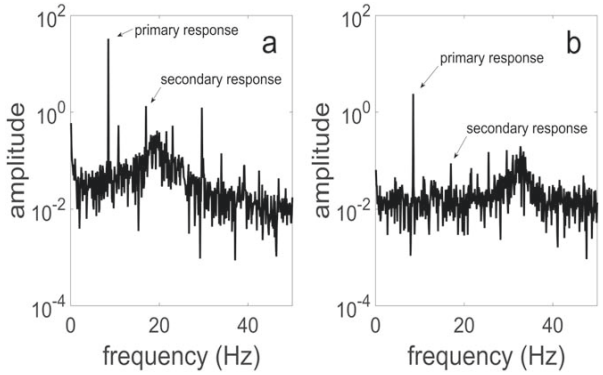

Figure 5. Dust particle pair driven at 8.5 Hz. (a) FFT of the sloshing coordinate. (b) FFT for the breathing coordinate.

confinements in equation (1) are calculated to be $k_1 = 6733\ \mathrm{s}^{-2}$ and $k_2 = 22\,368\ \mathrm{s}^{-2}$, $\omega_1 = 19.2$ Hz and $\omega_2 = 16.2$ Hz.

3.2. Experimental measurement of response curves

Primary and secondary responses can be determined experimentally by driving the particle pair at a frequency Ω and then calculating the FFT of the particles' motion in the decoupled coordinates $x_-(t)$ and $x_+(t)$. A representative example is shown in figure 5, where FFT's for both the sloshing coordinate (figure 5(a)) and breathing coordinate (figure 5(b)) are shown for a particle pair driven at 8.5 Hz. Strong peaks, the primary response, appear at 8.5 Hz (Ω) in both coordinates, accompanied by relatively weak peaks at the secondary response at 17 Hz (2Ω). Designating the amplitude of the peaks corresponding to the primary and secondary response at varying driving frequencies as $P(\Omega)$ and $S(\Omega)$, the primary and secondary response curves as a function of Ω can be obtained experimentally.

It is important to note that there appears to be a contradiction between the analytical solutions given in equations (9)–(12) and the experimental observations. For the analytical solutions, the responses at the natural frequencies ω_+ and ω_- are transient terms which decay as time increases. However, in experimental observations, these transient components remain throughout (figure 5). This contradiction is reconciled by noting that under actual experimental conditions, there are always thermal excitations (kicks) such that the response reaches a steady state.

4. Results

4.1. Determination of the particle–particle interaction to the nonlinear regime

The obtained experimental primary response curves can be fitted by the theoretical primary responses (as given by equations (9)–(10)). Figure 6 shows fits to the primary responses in sloshing (figure 6(a)) and breathing (figure 6(b)) coordinates under these conditions. Since the parameters ω_+ and ω_- have already been determined from the SMS, there are

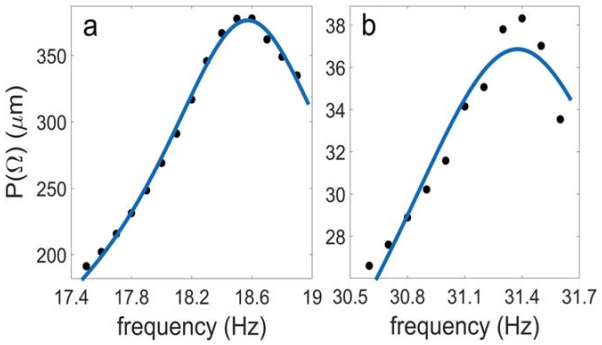

Figure 6. Primary response curves for (a) sloshing coordinate and (b) breathing coordinate. The points are experimental data while the lines are fits to the analytical solution (i.e. first terms in equations (9*a*) and (10*b*)).

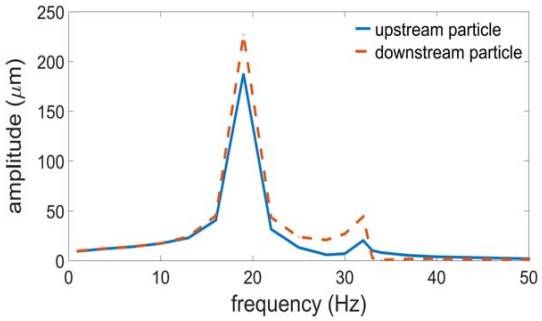

Figure 7. Experimental measurement of the oscillation amplitudes (primary responses) for both the upstream (blue solid line) and downstream particle (red dashed line).

only two parameters, μ and f_+ (f_-), left to be determined from each fit. As such, these fits yield a drag coefficient [47] of $\mu = 7.7\ \mathrm{s}^{-1}$ within the primary sloshing region and $\mu = 9.0\ \mathrm{s}^{-1}$ for the primary breathing region, in agreement with the value of $\mu = 8.5 \pm 0.9\ \mathrm{s}^{-1}$ as measured employing a free fall technique [48, 49]. This allows values for f_+ and f_- to be determined from the fit as $f_+ = 0.67 \times 10^5\ \mu\mathrm{m\,s}^{-2}$ and $f_- = 3.34 \times 10^5\ \mu\mathrm{m\,s}^{-2}$, respectively.

Before these fits can be employed to determine the secondary responses, the relative phase of the decoupled driving forces $f_1 \exp(\mathrm{i}\Omega t)$ and $f_2 \exp(\mathrm{i}\Omega t)$ must first be identified, i.e. whether f_1 and f_2 are of the same or opposite sign. This clarification can be made by taking advantage of the following experimental observation: at lower driving frequencies the magnitude of the oscillation of the upstream particle is larger than that of the downstream particle, while at higher frequencies the situation is reversed. Figure 7 shows experimentally measured oscillation amplitudes for both the upstream and downstream particles. The blue line corresponds to the upstream particle $x_1(t)$ while the dashed red line corresponds to the downstream particle $x_2(t)$. A transition point can be observed at a driving frequency of approximately 34 Hz.

This phenomenon can be explained theoretically by solving the equations of motion for two linear forced coupled oscillators (see equation (1) without the nonlinear interaction

terms $k_1'(x_1 - x_2)^2$ and $k_2'(x_1 - x_2)^2$). The nonlinear terms have little effect on the primary responses observed under small excitation amplitudes as discussed in the discussion section. The ratio R between the response amplitudes of the upstream and downstream particle can thus be derived from the linear equations of motion as

$$R = \frac{\{[F_1(-\Omega^2 + k_2 + \omega_2^2) + k_1F_2][F_2(-\Omega^2 + k_1 + \omega_1^2) + k_2F_1] + \mu^2\Omega^2F_1F_2\}}{[F_2(-\Omega^2 + k_1 + \omega_1^2) + k_2F_1]^2 + (\mu\Omega F_2)^2} + \mathrm{i}\mu\Omega\frac{\{F_1[F_2(-\Omega^2 + k_1 + \omega_1^2) + k_2F_1] - F_2[F_1(-\Omega^2 + k_2 + \omega_2^2) + k_1F_2]\}}{[F_2(-\Omega^2 + k_1 + \omega_1^2) + k_2F_1]^2 + (\mu\Omega F_2)^2}. \quad (13)$$

For simplification we drop the damping terms in equation (13). This can be justified since the damping is of the same order of magnitude as the nonlinear force contribution. Therefore, neglecting the damping does not qualitatively affect the result. By doing so, the amplitude ratio now reduces to

$$R = \frac{\eta(-\Omega^2 + k_2 + \omega_2^2) + k_1}{(-\Omega^2 + k_1 + \omega_1^2) + \eta k_2}, \quad (14)$$

where $\eta = \frac{F_1}{F_2}$ is defined as the ratio between the amplitudes of the excitation forces. Once f_+ and f_- are determined from fitting the measured primary response (as shown in figure 6), F_1 and F_2 are found using equation (3*c*). For the response fits shown in figure 6, this allows η to be calculated to be 0.62 when f_+ and f_- are of the opposite sign (i.e. out of phase case) and 1.1 when f_+ and f_- are of the same sign (i.e. in phase case). Based on the parameters k_1, k_2, ω_1 and ω_2 determined by employing the SMS method, the frequency ranges where the oscillation amplitude for the upstream particle is larger than that for the downstream particle (i.e. $R > 1$) can now be calculated from equation (14). This frequency range takes different form depending on the value of η, and it is also conditional on whether $\omega_1^2 - \omega_2^2$ is greater or less than $\frac{1-\eta}{\eta}(k_1 + \eta k_2)$:

$$\Omega^2 \in \left(-\infty, \frac{\omega_1^2 - \eta\omega_2^2}{1 - \eta}\right) \bigcup (k_1 + \eta k_2 + \omega_1^2, +\infty), \ \eta > 1, \quad (15a)$$

$$\Omega^2 \in \left(\frac{\omega_1^2 - \eta\omega_2^2}{1 - \eta}, k_1 + \eta k_2 + \omega_1^2\right), \ 0 < \eta < 1. \quad (15b)$$

For the situation $\eta > 1$ (i.e. in-phase driving), $\omega_1^2 - \omega_2^2$ is found to be greater than $\frac{1-\eta}{\eta}(k_1 + \eta k_2)$ based on the experimental parameters derived for k_1, k_2, ω_1, and ω_2. The corresponding frequency range that the oscillation of the upstream particle is larger than that for the downstream particle ($R > 1$) is predicted by equation (15*a*) to be $\Omega > 34$ Hz, while for the situation $0 < \eta < 1$ (i.e. out of phase driving), $\omega_1^2 - \omega_2^2$ is less than $\frac{1-\eta}{\eta}(k_1 + \eta k_2)$ leading to a frequency range described in equation (15*b*) as $24\ \mathrm{Hz} \leqslant \Omega \leqslant 30\ \mathrm{Hz}$. Thus the predicted result for in-phase driving agrees with the observed experimental response shown in figure 7, and we can conclude that f_+ and f_- are of the same sign. As a side result, it is determined that the driving force on the upstream particle is greater than that acting on the downstream particle, $F_1 > F_2$, in agreement with results reported by Carstensen *et al* [10].

With f_+ and f_- now determined, the experimentally determined secondary response curve can be compared to the theoretically derived secondary response (equations (11) and (12)). The fits with experiment are shown for the sloshing coordinate with $\Omega \approx \frac{1}{2}\omega_-$ in figure 8(a), while the fit for the breathing coordinate with $\Omega \approx \frac{1}{2}\omega_+$ is shown in figure 8(b). Since the secondary responses are smaller than our camera resolution of 9.0 μm per pixel, the errorbar caused by this uncertainty in measurement is shown in figure 8. It is noticed that the measurements below 1 μm will be considered as less reliable than those above 1 μm due to the nonlinearity of the measurement (see appendix B). Here the free parameters in each fit are g_1 and g_2, which are determined to be $g_1 = 31.1\ \mu\mathrm{m}^{-1}\,\mathrm{s}^{-2}$ and $g_2 = 283.2\ \mu\mathrm{m}^{-1}\,\mathrm{s}^{-2}$ respectively. The nonlinear coefficients k_1' and k_2' are then in turn calculated to be $-253.4\ \mu\mathrm{m}^{-1}\,\mathrm{s}^{-2}$ and $-364.6\ \mu\mathrm{m}^{-1}\,\mathrm{s}^{-2}$ from equation (3*a*).

4.2. Numerical results

Additional simulations were conducted to validate the calculated values for k_1' and k_2' above. In this case, particle motions were simulated using a velocity Verlet algorithm based on the parameters ω_1, ω_2, k_1 and k_2 measured from the SMS technique and μ, F_1, F_2, k_1' and k_2' calulated from the response fits. The particle motion was simulated for for purely linear interactions ($k_1' = k_2' = 0$) as well as nonlinear interactions. The resulting time series for the particle positions was then processed using the same approach as for the experimental data to obtain simulated response functions. The primary responses for the $x_1(t)$ and $x_2(t)$ coordinates are shown in figure 9. As can be seen, the simulation agrees well with experiment (figure 7) and successfully reproduces the transition phenomenon at around 34 Hz. The primary responses with nonlinear interactions exhibit only slight deviations from those with only linear interactions. This supports the previous argument that for small excitation amplitudes, the primary response is only minimally affected by the nonlinear interaction.

Secondary responses obtained from simulations with nonlinear interaction are indicated by the dashed line in figure 10, for $\Omega \approx \omega_-$ (figure 10(a)) and $\Omega \approx \omega_+$ (figure 10(b)) for both the breathing ($x_+(t)$, red curves) and

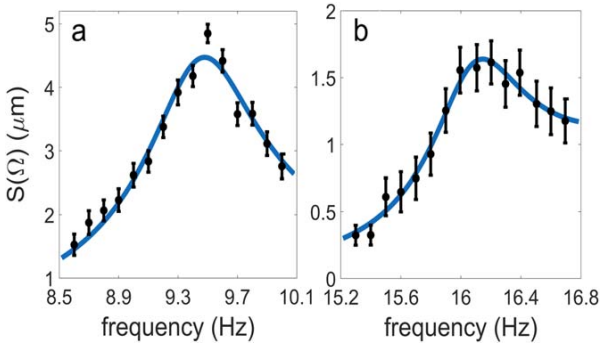

Figure 8. Fits for the measured secondary responses (a) in the sloshing coordinate at $\frac{1}{2}\omega_-$ and (b) breathing coordinate at $\frac{1}{2}\omega_+$ to the analytical response curves. The points show experimental data while the solid lines are fits using the theoretical solutions (i.e. first terms in equations (11*a*) and (12*b*)). The errorbars are due to the measurement uncertainty caused by the resolution of the camera which is 9 μm per pixel.

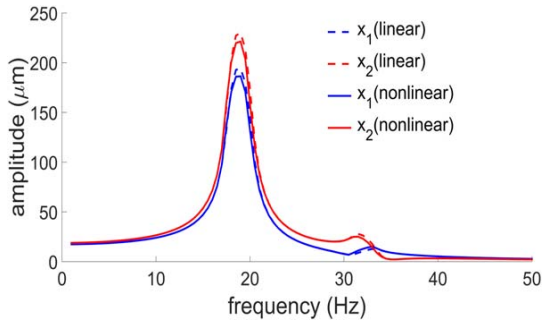

Figure 9. Simulated response of upstream (blue) and downstream (red) particles. Solid lines show the results including the nonlinear interaction terms, while the dashed lines show the response using only linear interaction terms.

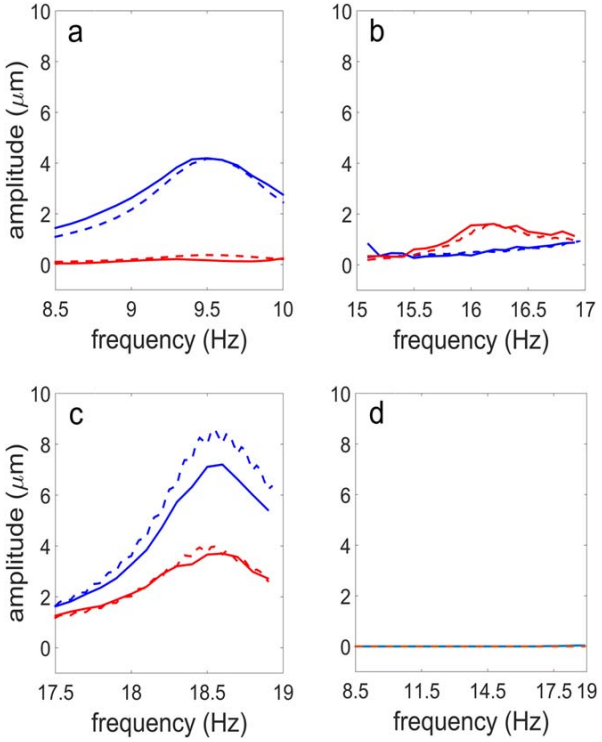

Figure 10. Simulated secondary responses for (a) the secondary sloshing region near $\frac{1}{2}\omega_-$ (around 9.5 Hz), (b) the secondary breathing region near $\frac{1}{2}\omega_+$ (around 16 Hz) and (c) the primary sloshing region near ω_- (around 18.5 Hz). Simulations including nonlinear interactions are plotted as dashed lines while experimental measurements are plotted as solid lines. Simulations which do not include nonlinear interactions ($k_1' = 0$, $k_2' = 0$) are plotted in figure 10 (d). Lines plotted in blue represent sloshing coordinates and those plotted in red represent breathing coordinates.

sloshing ($x_-(t)$, blue curves) coordinates. The consistency of the simulation with experimental measurement (solid curves) confirms our calculation of the nonlinear coefficients k_1' and k_2'. Figure 10(d) shows the simulation without considering nonlinear interaction, i.e. $k_1' = 0$ and $k_2' = 0$. As can be seen, when nonlinear interactions are not considered, there is no secondary response excited, indicating that secondary responses are purely caused by the nonlinear interactions. It is also interesting to note that both experiment and simulation show a secondary response in the breathing coordinate when the excitation frequency is around 18.5 Hz (the sloshing frequency ω_-) as shown in figure 10(c). Therefore, the breathing coordinate responds to the sloshing excitation. This is most likely a consequence of mode coupling in the nonlinear regime.

5. Discussion

In this research, the restoring force due to the sheath potential is considered to be linear, leaving the source of nonlinearity to be attributed to the particle–particle interaction ($k_1'(x_1 - x_2)^2$ and $k_2'(x_2 - x_1)^2$) only. This assumption can be justified based on the findings of Tomme *et al* [50, 51], which showed that particle motion can be extremely well modeled by a damped harmonic oscillator for amplitudes approaching 20% of the sheath width. In this research, small particle vibration amplitudes are ensured through application of a low driving amplitude (1 V) through an attenuator. This provides a maximum vibration amplitude (appearing at the sloshing resonance) of less than 250 μm, which is estimated to be approximately 2% of the total sheath width. (The sheath edge is estimated to be at the plasma glow maxima.) As such, it is safe to assume a parabolic sheath potential (i.e. a linear electric field) and to ignore the effect of charge fluctuations.

Additionally, the maximum vibration amplitude in the breathing coordinate is less than 40 μm, which is small compared to the equilibrium interparticle spacing which is approximately 140 μm. Therefore, in theory, nonlinear effects in the particle–particle interaction beyond the quadratic term can be ignored. With this approximation both the theory (equations (9) and (10)) and simulation (figure 9) show that the primary response in both sloshing and breathing

coordinates very weakly depends on the nonlinear coefficients k_1' and k_2'. Experimental results are in agreement with this conclusion, validiating the choice of neglecting higher order nonlinear terms.

Further increasing the excitation amplitude produces 'spring hardening' in the breathing coordinate, i.e. the resonance frequency shifts towards higher frequencies. This occurs as a consequence of a cubic nonlinearity. In fact, even under small excitations (e.g. the excitation in the presented experiment), the breathing mode is still slightly affected by these cubic nonlinearities, which is the reason that the primary breathing fit (figure 6(b)) is not as accurate as the primary sloshing fit (figure 6(a)). Interestingly, the spring hardening effect only appears in the breathing coordinate, while in the sloshing coordinate there is no obvious frequency shift. Since the breathing coordinate characterizes the particles' relative motion, this also confirms that the nonlinearity of the system arises from the particle–particle interaction rather than from the sheath, as discussed above. The situation of large excitation (significant spring hardening in the breathing coordinate created by the cubic nonlinearity) will be examined in future experiments.

Although the excitation (vibration amplitude) observed in the current research is small, secondary responses in both the sloshing and breathing coordinates are clearly seen. Since both theory and simulation show that these vanish for purly linear interactions, they serve as a signature of nonlinear particle–particle interactions.

It may be helpful here to compare our results to the case of a reciprocal particle–particle interaction and identical background confinement for both particles. Considering a reciprocal interaction ($k_1 = k_2 = k$, $k_1' = -k_2' = k'$) and identical confinement ($\omega_1 = \omega_2$) in equation (1), the modes are now orthogonal and $\alpha_+ = -1$ while $\alpha_- = 1$. For the ideal situation where both particles are driven identically, i.e. $F_1 = F_2 = F$, the external driving term disappears in the breathing coordinate while the driving magnitude equals $2F$ in the sloshing coordinate (equation (3*c*)). In this case, the breathing mode cannot be excited. However, in an actual experimental situation, any difference in the driving force or nonreciprocity in the particle–particle interaction can cause the breathing mode to become excited, in contrast to the result reported by Prior *et al* [52]. As seen in equation (3*c*), even when α_+/α_- deviates from -1 /1 (as is the case in the actual experiment), the effective driving force f_- is still much larger than f_+, explaining the much stronger primary response in the sloshing coordinate than in the breathing coordinate (see figure 6).

For $F_1 \neq F_2$, excitations of the two modes for a system with reciprocal interaction and an identical symmetric background confinement obey

$$\ddot{x}_+ + \mu\dot{x}_+ + \omega_+^2 x_+ + 2k'x_+^2 = (F_1 - F_2)\exp(\mathrm{i}\Omega t),$$
$$\ddot{x}_- + \mu\dot{x}_- + \omega_-^2 x_- = (F_1 + F_2)\exp(\mathrm{i}\Omega t). \quad (16)$$

In this case, nonlinear terms only appear for the breathing coordinate, while the equation of motion for the sloshing coordinate remains linear. Comparing equation (16) to (2), we can conclude that it is the non-reciprocal interaction and the non-identical background confinement that couples the sloshing and breathing modes in a nonlinear manner. The secondary excitation observed in the sloshing coordinate is thus purely a consequence of this nonlinear coupling.

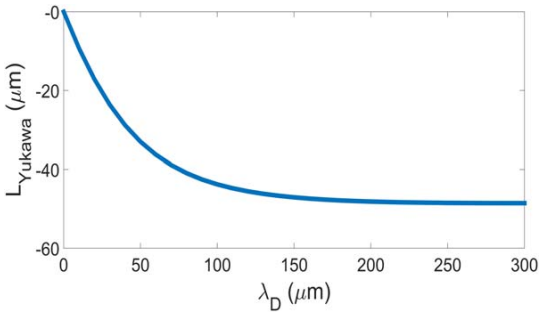

Figure 11. The dependence of L_{Yukawa} on the Debye length λ_D for a Yukawa force with interparticle spacing $d = 140$ μm. As the Debye length increases, L_{Yukawa} asymptotically approaches the value for a Coulomb interaction with $L_{\mathrm{Coulomb}} = -47$ μm.

The ion wake causes the particle–particle interaction to be non-reciprocal. The wake effect (in the direction of the ion flow) can be determined by examining the interaction force near the particle equilibrium positions. Since the deviation from the equilibrium separation is small, the interaction force can be approximated by a Taylor series expansion whose first and second derivatives are characterized by $k_{1(2)}$ and $k_{1(2)}'$. We define the nonlinearity length $L_1 = \frac{k_1}{k_1'}$ and $L_2 = \frac{k_2}{k_2'}$ as the ratio of the linear coefficients k_1, k_2 to the second order nonlinear coefficients k_1', k_2'. This nonlinearity length L can be used as a measurement of nonlinearity scale for the particle–particle interaction. In this case, for the upstream force $L_1 = \frac{k_1}{k_1'} = -28$ μm and for the downstream force $L_2 = \frac{k_2}{k_2'} = -65$ μm. Previously, no particular force model was assumed to determine the coupling coefficients k_1, k_2, k_1' and k_2'. Now we consider the force between two particles which interact through a Yukawa potential $\Phi = \frac{kQ}{r}\exp\left(\frac{\lambda_D}{r}\right)$. We calculate L for a Yukawa interaction as a function of the Debye length λ_D:

$$L_{\mathrm{Yukawa}} = -\frac{2d\lambda_D^3 + 2d^2\lambda_D^2 + d^3\lambda_D}{6\lambda_D^3 + 6d\lambda_D^2 + 3d^2\lambda_D + d^3}, \quad (17)$$

where d is the inter-particle spacing at equilibrium (approximately 140 μm for this experiment). This L_{Yukawa} approaches an asymptotic value of $L = -\frac{d}{3}$ for large Debye length, which coresponds to the Coulomb interaction potential (i.e. $L_{\mathrm{Coulomb}} = -\frac{d}{3}$). Figure 11 shows nonlinearity length L_{Yukawa} for a particle separation $d = 140$ μm as a function of λ_D. It can be seen that the value for the upstream particle, $L_1 = -28$ μm falls in the range where the Debye length λ_D equals approximately $1/3$ of the inter-particle spacing, while the value for downstream nonlinearity length $L_2 = -65$ μm exceeds the asymptotic value $L = -47$ μm (corresponding to

the Coulomb interaction). Thus, due to the ion wake, the downstream force is no longer a simple Yukawa or Coulomb interaction, even though the upstream force can still be described as an effective Yukawa interaction, in agreement with results reported in [25, 26, 53, 54]. Furthermore, since $|L_1| < |L_2|$, it appears that the downstream interaction is more linear than the upstream. This implies that when the paired particles are at their equillibrium positions, the more linear restoring field for the downstream particle (effectively from the particle–particle interaction), results in more stable oscillations for the downstream particle.

6. Conclusions

A method to analyze nonlinear particle–particle interactions for a paired particle structure aligned with the ion flow in a complex plasma by experimentally measuring the nonlinear amplitude-frequency response curves has been presented. The method relies on examining the particle motion in a new coordinate system, the 'breathing' and 'sloshing' coordinates. Rewriting the system of equations for two coupled, forced oscillators in terms of these coordinates allows the sloshing and breathing modes to be linearly decoupled, as shown in equation (2) and illustrated in figure 3. The coupling in the nonlinear term is determined to result from the non-reciprocal particle interaction caused by the ion wake.

Multiple-scale analysis is used to solve the system of nonlinear coupled equations, and the motion is investigated for the primary response region (frequency near the driving frequency Ω) and the secondary response (frequency near 2Ω). The primary response in the breathing and sloshing coordinates are found to be independent of the nonlinear parameters (equations (9*a*) and (10*b*)), which only appear in the equations for the secondary response (equations (11*a*) and (12*b*)).

Amplitude-frequency response curves are obtained experimentally by applying a sinusoidally varying voltage to the lower electrode to drive the particles in the vertical direction. Fitting the primary response curve, determined from the amplitude of the FFT of the motion in the breathing and sloshing coordinates at the driving frequency Ω, with the analytical expression for the primary response allows the magnitude of the driving force and the damping parameter to be determined (figure 6). In turn, fitting the experimentally measured secondary response curves (figure 8) allows the coefficients of the nonlinear coupling to be found.

Simulations of the particle motion using these measured parameters confirmed that the nonlinear terms contribute very little to the primary response of the system (figure 9), whereas excluding the nonlinear terms from the interaction completely eliminates the secondary response (figure 10). Thus, the existence of the secondary response can be taken as a signature of the nonlinearity present in the system. Non-reciprocal interactions or differences in the background confinement, as would be expected for a particle pair with the interaction mediated by the ion wake, results in equations of motion which are similar to the coupled driven oscillators (see equations (2) and (16)). In this case, the coupling in the nonlinear term is determined to result from the apparent non-reciprocal particle–particle interaction caused by the ion wake. Further analysis shows that the nonlinear length scale, defined as the ratio of the coefficients of the linear and nonlinear terms, is greater for the downstream particle. Thus the restoring force acting on the downstream particle is more linear than that acting on the upstream particle, stabilizing the oscillations of the downstream particle.

Acknowledgments

Support from NASA grant number 1571701 and NSF grant number 1740203 is gratefully acknowledged.

Appendix A. Full derivation of the solutions at the primary breathing region

Consider the driving frequency near ω_+, i.e. $\Omega = \omega_+ + \delta\epsilon$. Writting out the drag force and the driving force at resonance to the same order in the nonliner terms (i.e. $\mu = \epsilon\mu'$, $f_+ = \epsilon^2 f_+'$, $f_- = \epsilon f_-'$), the equations of motion take the following form

$$\ddot{x}_+ + \epsilon\mu'\dot{x}_+ + \omega_+^2 x_+ + g_1(c_1x_+ - c_2x_-)^2 = \epsilon^2 f_+' \exp(\mathrm{i}\Omega t) + \text{c.c.}, \tag{A1}$$

$$\ddot{x}_- + \epsilon\mu'\dot{x}_- + \omega_-^2 x_- + g_2(c_1x_+ - c_2x_-)^2 = \epsilon f_-' \exp(\mathrm{i}\Omega t) + \text{c.c.} \tag{A2}$$

By substituting in the test solution

$$x_+(t_0, t_1) = \epsilon x_{+1}(t_0, t_1) + \epsilon^2 x_{+2}(t_0, t_1), \tag{A3}$$

$$x_-(t_0, t_1) = \epsilon x_{-1}(t_0, t_1) + \epsilon^2 x_{-2}(t_0, t_1), \tag{A4}$$

where $t_0 = t$ and $t_1 = \epsilon t_0$, the equations of motion to second order in ϵ are given by

$$\left(\frac{\partial^2}{\partial t_0^2} + 2\epsilon\frac{\partial^2}{\partial t_0\partial t_1} + \epsilon^2\frac{\partial^2}{\partial t_1^2}\right)(\epsilon x_{+1} + \epsilon^2 x_{+2}) + \epsilon\mu'\left(\frac{\partial}{\partial t_0} + \epsilon\frac{\partial}{\partial t_1}\right)(\epsilon x_{+1} + \epsilon^2 x_{+2}) + \omega_+^2(\epsilon x_{+1} + \epsilon^2 x_{+2}) + g_1[c_1(\epsilon x_{+1} + \epsilon^2 x_{+2}) - c_2(\epsilon x_{-1} + \epsilon^2 x_{-2})]^2 = \epsilon^2 f_+' \exp(\mathrm{i}\Omega t_0) + \text{c.c.}, \tag{A5}$$

$$\left(\frac{\partial^2}{\partial t_0^2} + 2\epsilon\frac{\partial^2}{\partial t_0\partial t_1} + \epsilon^2\frac{\partial^2}{\partial t_1^2}\right)(\epsilon x_{-1} + \epsilon^2 x_{-2}) + \epsilon\mu'\left(\frac{\partial}{\partial t_0} + \epsilon\frac{\partial}{\partial t_1}\right)(\epsilon x_{+1} + \epsilon^2 x_{+2}) + \omega_-^2(\epsilon x_{-1} + \epsilon^2 x_{-2}) + g_1[c_1(\epsilon x_{+1} + \epsilon^2 x_{+2}) - c_2(\epsilon x_{-1} + \epsilon^2 x_{-2})]^2 = \epsilon f_-' \exp(\mathrm{i}\Omega t_0) + \text{c.c.} \tag{A6}$$

The equations of motion are separated at different orders of ϵ, by equating all the terms of order of ϵ and ϵ^2.

To first order in ϵ, the equations of motion are

$$\frac{\partial^2}{\partial t_0^2}x_{+1} + \omega_+^2 x_{+1} = 0, \tag{A7}$$

$$\frac{\partial^2}{\partial t_0^2}x_{-1} + \omega_-^2 x_{-1} = f'_- \exp(\mathrm{i}\Omega t_0) + \text{c.c.}, \tag{A8}$$

with the solution to the first order

$$x_{+1} = A\exp(\mathrm{i}\omega_+ t_0) + \text{c.c.}, \tag{A9}$$

$$x_{-1} = B\exp(\mathrm{i}\omega_- t_0) + \frac{f'_-}{-\Omega^2 + \omega_-^2}\exp(\mathrm{i}\Omega t_0) + \text{c.c.} \tag{A10}$$

Equating the terms which are second order in ϵ yields

$$\frac{\partial^2}{\partial t_0^2}x_{+2} + \omega_+^2 x_{+2} = -2\frac{\partial^2}{\partial t_0 \partial t_1}x_{+1} - \mu'\frac{\partial}{\partial t_0}x_{+1} - g_1(c_1 x_{+1} - c_2 x_{-1})^2 + (f'_+\exp(\mathrm{i}\Omega t_0) + \text{c.c.}), \tag{A11}$$

$$\frac{\partial^2}{\partial t_0^2}x_{-2} + \omega_-^2 x_{-2} = -2\frac{\partial^2}{\partial t_0 \partial t_1}x_{-1} - \mu'\frac{\partial}{\partial t_0}x_{-1} - g_2(c_1 x_{+1} - c_2 x_{-1})^2. \tag{A12}$$

Substituting x_{+1} and x_{-1} given by (A9) and (A10) into (A11) and (A12)

$$\begin{aligned}\frac{\partial^2}{\partial t_0^2}x_{+2} + \omega_+^2 x_{+2} = {} & -2\mathrm{i}\omega_+\frac{\partial A}{\partial t_1}\exp(\mathrm{i}\omega_+ t_0) \\ & - \mu'\mathrm{i}\omega_+ A\exp(\mathrm{i}\omega_+ t_0) + f'_+\exp(\mathrm{i}\Omega t_0) \\ & - g_1\Big[c_1^2A^2\exp(\mathrm{i}2\omega_+ t_0) + c_2^2B^2\exp(\mathrm{i}2\omega_- t_0) \\ & - 2c_1c_2AB\exp(\mathrm{i}(\omega_+ + \omega_-)t_0) \\ & - 2c_1c_2AB^*\exp(\mathrm{i}(\omega_+ - \omega_-)t_0) \\ & - 2c_1c_2A\left(\frac{f'_-}{-\Omega^2 + \omega_-^2}\right)\exp(\mathrm{i}(\omega_+ + \Omega)t_0 \\ & - 2c_1c_2\left(\frac{f'_-}{-\Omega^2 + \omega_-^2}\right)\exp(\mathrm{i}(\omega_+ - \Omega)t_0) \\ & + 2c_2^2B\left(\frac{f'_-}{-\Omega^2 + \omega_-^2}\right)\exp(\mathrm{i}(\omega_- + \Omega)t_0) \\ & + 2c_2^2B\left(\frac{f'_-}{-\Omega^2 + \omega_-^2}\right)\exp(\mathrm{i}(\omega_- + \Omega)t_0) \\ & + c_2^2\left(\frac{f'_-}{-\Omega^2 + \omega_-^2}\right)^2\exp(\mathrm{i}2\Omega t_0) \\ & + c_1^2AA^* + c_2^2BB^* + c_2^2\left(\frac{f'_-}{-\Omega^2 + \omega_-^2}\right)^2\Big] + \text{c.c.},\end{aligned} \tag{A13}$$

$$\begin{aligned}\frac{\partial^2}{\partial t_0^2}x_{-2} + \omega_-^2 x_{-2} = {} & -2\mathrm{i}\omega_-\frac{\partial B}{\partial t_1}\exp(\mathrm{i}\omega_- t_0) \\ & - \mu'\mathrm{i}\omega_- B\exp(\mathrm{i}\omega_- t_0) \\ & - \mu\mathrm{i}\Omega\left(\frac{f'_-}{-\Omega^2 + \omega_-^2}\right)\exp(\mathrm{i}\Omega t_0) - g_1\Big[c_1^2A^2\exp(\mathrm{i}2\omega_+ t_0) \\ & + c_2^2B^2\exp(\mathrm{i}2\omega_- t_0) \\ & - 2c_1c_2AB\exp(\mathrm{i}(\omega_+ + \omega_-)t_0) \\ & - 2c_1c_2AB^*\exp(\mathrm{i}(\omega_+ - \omega_-)t_0) \\ & - 2c_1c_2A\left(\frac{f'_-}{-\Omega^2 + \omega_-^2}\right)\exp(\mathrm{i}(\omega_+ + \Omega)t_0) \\ & - 2c_1c_2\left(\frac{f'_-}{-\Omega^2 + \omega_-^2}\right)\exp(\mathrm{i}(\omega_+ - \Omega)t_0) \\ & + 2c_2^2B\left(\frac{f'_-}{-\Omega^2 + \omega_-^2}\right)\exp(\mathrm{i}(\omega_- + \Omega)t_0) \\ & + 2c_2^2B\left(\frac{f'_-}{-\Omega^2 + \omega_-^2}\right)\exp(\mathrm{i}(\omega_- - \Omega)t_0) \\ & + c_2^2\left(\frac{f'_-}{-\Omega^2 + \omega_-^2}\right)^2\exp(\mathrm{i}2\Omega t_0) + c_1^2AA^* + c_2^2BB^* \\ & + c_2^2\left(\frac{f'_-}{-\Omega^2 + \omega_-^2}\right)^2\Big] + \text{c.c.}\end{aligned} \tag{A14}$$

Since $\exp(\mathrm{i}\Omega t_0) = \exp(\mathrm{i}w_+ t_0 + \delta t_1)$, where $\Omega = \omega_+ + \delta\epsilon$, then (A13) and (A14) become:

$$\begin{aligned}\frac{\partial^2}{\partial t_0^2}x_{+2} + \omega_+^2 x_{+2} = {} & \Big[-2\mathrm{i}\omega_+\frac{\partial A}{\partial t_1} - \mu'\mathrm{i}\omega_+ A \\ & + f'_+\exp(\mathrm{i}\delta t_1)\Big]\exp(\mathrm{i}\omega_+ t_0) \\ & - g_1\Big[c_1^2A^2 + c_2^2\left(\frac{f'_-}{-\Omega^2 + \omega_-^2}\right)^2\exp(\mathrm{i}2\delta t_1) \\ & - 2c_1c_2A\left(\frac{f'_-}{-\Omega^2 + \omega_-^2}\right)\exp(\mathrm{i}\delta t_1)\Big]\exp(\mathrm{i}2\omega_+ t_0) \\ & - g_1\Big[2c_2^2B\left(\frac{f'_-}{-\Omega^2 + \omega_-^2}\right)\exp(\mathrm{i}\delta t_1) - 2c_1c_2AB\Big] \\ & \times\exp(\mathrm{i}(\omega_+ + \omega_-)t_0) \\ & - g_1\Big[2c_2^2B^*\left(\frac{f'_-}{-\Omega^2 + \omega_-^2}\right)\exp(\mathrm{i}\delta t_1) - 2c_1c_2AB^*\Big] \\ & \times\exp(\mathrm{i}(\omega_+ - \omega_-)t_0) \\ & - g_1\Big[c_1^2AA^* + c_2^2BB^* + c_2^2\left(\frac{f'_-}{-\Omega^2 + \omega_-^2}\right)^2 \\ & - 2c_1c_2A\left(\frac{f'_-}{-\Omega^2 + \omega_-^2}\right)\exp(-\mathrm{i}\delta t_1)\Big] \\ & - g_1c_2^2B^2\exp(\mathrm{i}2\omega_- t_0) + \text{c.c.}\end{aligned} \tag{A15}$$

$$\frac{\partial^2}{\partial t_0^2}x_{-2} + \omega_-^2 x_{-2} = \left(-2\mathrm{i}\omega_-\frac{\partial B}{\partial t_1} - \mu'\mathrm{i}\omega_- B\right)\exp(\mathrm{i}\omega_- t_0)$$
$$- \mu'\mathrm{i}\Omega\left(\frac{f_-}{-\Omega^2+\omega_-^2}\right)\exp(\mathrm{i}\delta t_1)\exp(\mathrm{i}\omega_+ t_0)$$
$$- g_2\left[c_1^2A^2 + c_2^2\left(\frac{f'_-}{-\Omega^2+\omega_-^2}\right)^2\exp(\mathrm{i}2\delta t_1)\right.$$
$$\left. - 2c_1c_2A\left(\frac{f'_-}{-\Omega^2+\omega_-^2}\right)\exp(\mathrm{i}\delta t_1)\right]\exp(\mathrm{i}2\omega_+ t_0)$$
$$- g_2\left[2c_2^2B\left(\frac{f'_-}{-\Omega^2+\omega_-^2}\right)\exp(\mathrm{i}\delta t_1) - 2c_1c_2AB\right]$$
$$\times \exp(\mathrm{i}(\omega_+ + \omega_-)t_0)$$
$$- g_2\left[2c_2^2B^*\left(\frac{f'_-}{-\Omega^2+\omega_-^2}\right)\exp(\mathrm{i}\delta t_1) - 2c_1c_2AB^*\right]$$
$$\times \exp(\mathrm{i}(\omega_+ - \omega_-)t_0)$$
$$- g_2\left[c_1^2AA^* + c_2^2BB^* + c_2^2\left(\frac{f'_-}{-\Omega^2+\omega_-^2}\right)^2\right.$$
$$\left. - 2c_1c_2A\left(\frac{f'_-}{-\Omega^2+\omega_-^2}\right)\exp(-\mathrm{i}\delta t_1)\right]$$
$$- g_2c_2^2B^2\exp(\mathrm{i}2\omega_- t_0) + \mathrm{c.c.} \tag{A16}$$

To ensure that there are no secular terms in the equations of motion for x_{+2} (A15) and x_{-2} (A16), the resonant terms on the right hand side of (A15) and (A16) are forced to be 'zero', allowing the coefficients A and B to be determined from

$$-2\mathrm{i}\omega_+\frac{\partial A}{\partial t_1} - \mu'\mathrm{i}\omega_+ A + f'_+\exp(\mathrm{i}\delta t_1) = 0, \tag{A17}$$

$$-2\mathrm{i}\omega_-\frac{\partial B}{\partial t_1} - \mu'\mathrm{i}\omega_- B = 0, \tag{A18}$$

with the solutions

$$A = \frac{f'_+}{\mathrm{i}\omega_+(\mu' + \mathrm{i}2\delta)}\exp(\mathrm{i}\delta t_1) + c\exp\left(-\frac{\mu' t_1}{2}\right), \tag{A19}$$

$$B = c'\exp\left(-\frac{\mu' t_1}{2}\right). \tag{A20}$$

Thus, the solutions to first order in ϵ are found to be

$$x_+ = \frac{-f_+}{\omega_+[\mu^2 + 4(\Omega-\omega_+)^2]^{\frac{1}{2}}}$$
$$\times \exp\left(\mathrm{i}\left[\Omega t + \mathrm{arctg}\left(\frac{\mu}{2(\Omega-\omega_+)}\right)\right]\right)$$
$$+ C\exp\left(-\frac{\mu t_1}{2} + \mathrm{i}\omega_+ t\right) + \mathrm{c.c.}, \tag{A21}$$

$$x_- = \frac{f_-}{-\Omega^2+\omega_-^2}\exp(\mathrm{i}\Omega t) + C'\exp\left(-\frac{\mu t_1}{2} + \mathrm{i}\omega_- t\right) + \mathrm{c.c.}, \tag{A22}$$

where C and C' are constants depending on the initial conditions and 'cc' stands for the complex conjugate. The solutions for the other frequency regions are derived in a similar manner.

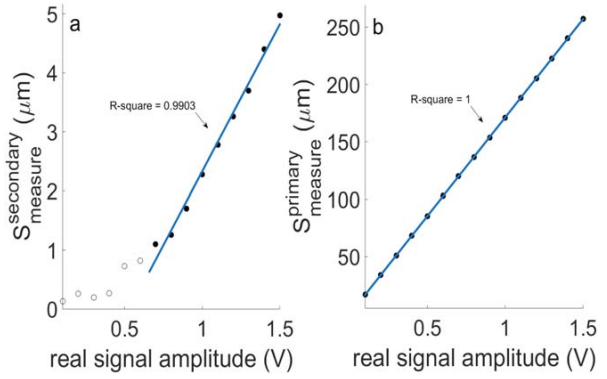

Figure B1. Calibration for (a) the secondary response measurement and (b) the primary response measurement.

Appendix B. Linearity of the measurement

To validate the linearity of the measurement for small responses (e.g. secondary responses are measured in the sub-pixel resolution), a calibration has been conducted between measured responses and real signal amplitudes. As shown in figure B1(a), measured secondary responses above 1 μm (solid circles) show a good linear dependence on real signal amplitude, while those below 1 μm (hollow circles), this dependency becomes less linear especially when the measured value is below 0.3 μm. Thus, measurement of the secondary response below 1 μm should be considered as less reliable due to nonlinearity of the measurement. Figure B1(b) shows the calibration of the primary responses where the measurement is verified to be linear.

ORCID iDs

Zhiyue Ding https://orcid.org/0000-0003-1554-5911

References

[1] Fortov V, Ivlev A, Khrapak S, Khrapak A and Morfill G 2005 *Phys. Rep.* **421** 1
[2] Melzer A, Schweigert V A, Schweigert I V, Homann A, Peters S and Piel A 1996 *Phys. Rev.* E **54** R46
[3] Schweigert V A, Schweigert I V, Melzer A, Homann A and Piel A 1996 *Phys. Rev.* E **54** 4155
[4] Schweigert V A, Schweigert I V, Melzer A, Homann A and Piel A 1998 *Phys. Rev. Lett.* **80** 5345
[5] Melzer A, Schweigert V A and Piel A 1999 *Phys. Rev. Lett.* **83** 3194
[6] Melzer A, Schweigert V A and Piel A 2000 *Phys. Scr.* **61** 494
[7] Hebner G A, Riley M E and Marder B M 2003 *Phys. Rev.* E **68** 016403
[8] Samarian A A, Vladimirov S V and James B W 2005 *Phys. Plasmas* **12** 022103

[9] Carstensen J, Greiner F and Piel A 2012 *Phys. Rev. Lett.* **109** 135001
[10] Zobnin A V, Nefedov A P, Sinel'shchikov V A, Sinkevich O A, Usachev A D, Filinov V S and Fortov V E 2000 *Plasma Phys. Rep.* **26** 415
[11] Melzer A 2001 *Plasma Sources Sci. Technol.* **10** 303
[12] Lapenta G 1999 *Phys. Plasmas* **6** 1442
[13] Verboncoeur J P 2005 *Plasma Phys. Control. Fusion* **47** A231
[14] Miloch W J, Kroll M and Block D 2010 *Phys. Plasmas* **17** 103703
[15] Hutchinson I H 2011 *Phys. Plasmas* **18** 032111
[16] Hutchinson I H 2011 *Phys. Rev. Lett.* **107** 095001
[17] Hutchinson I H 2012 *Phys. Rev.* E **85** 066409
[18] Miloch W J and Block D 2012 *Phys. Plasmas* **19** 123703
[19] Piel A 2011 *Phys. Plasmas* **18** 073704
[20] Lampe M, Röcker T B, Joyce G, Zhdanov S K, Ivlev A V and Morfill G E 2012 *Phys. Plasmas* **19** 113703
[21] Piel A 2017 *Phys. Plasmas* **24** 033712
[22] Matyash K, Schneider R, Ikkurthi R, Lewerentz L and Melzer A 2010 *Plasma Phys. Control. Fusion* **52** 124016
[23] Ikkurthi V R, Matyash K, Melzer A and Schneider R 2010 *Phys. Plasmas* **17** 103712
[24] Joyce G, Lampe M and Ganguli G 2001 *IEEE Trans. Plasma Sci.* **29** 238
[25] Jenko F, Joyce G and Thomas H M 2005 *Phys. Plasmas* **12** 022309
[26] Ludwig P, Miloch W J, Kählert H and Bonitz M 2012 *New J. Phys.* **14** 053016
[27] Laut I, Räth C, Zhdanov S K, Nosenko V, Morfill G E and Thomas H M 2017 *Phys. Rev. Lett.* **118** 075002
[28] Melandso F and Goree J 1996 *J. Vac. Sci. Technol.* A **14** 511
[29] Melzer A 2014 *Phys. Rev.* E **90** 053103
[30] Jung H, Greiner F, Asnaz O H, Carstensen J and Piel A 2015 *Phys. Plasmas* **22** 053702
[31] Steinberg V, Sütterlin R, Ivlev A V and Morfill G 2001 *Phys. Rev. Lett.* **86** 4540
[32] Kompaneets R, Vladimirov S V, Ivlev A V, Tsytovich V and Morfill G 2006 *Phys. Plasmas* **13** 072104
[33] Samarian A A and Vladimirov S V 2009 *Contrib. Plasma Phys.* **49** 260
[34] Qiao K, Matthews L S and Hyde T W 2010 *IEEE Trans. Plasma Sci.* **38** 826
[35] Nosenko V, Ivlev A V, Kompaneets R and Morfill G 2014 *Phys. Plasmas* **21** 113701
[36] Kong J, Hyde T W, Harris B, Qiao K and Carmona-Reyes J 2009 *IEEE Trans. Plasma Sci.* **37** 1620
[37] Kong J, Qiao K, Matthews L S and Hyde T W 2014 *Phys. Rev.* E **90** 013107
[38] Mukhopadhyay A K and Goree J 2012 *Phys. Rev. Lett.* **109** 165003
[39] Mukhopadhyay A K and Goree J 2014 *Phys. Rev.* E **90** 013102
[40] Ivlev A V, Sütterlin R, Steinberg V, Zuzic M and Morfill G 2000 *Phys. Rev. Lett.* **85** 4060
[41] Zafiu C, Melzer A and Piel A 2001 *Phys. Rev.* E **63** 066403
[42] Wang Y-N, Hou L-J and Wang X 2002 *Phys. Rev. Lett.* **89** 155001
[43] Resendes D P, Sorasio G and Shukla P K 2001 *Phys. Scr.* **T98** 87
[44] Sorasio G, Resendes D P and Shukla P K 2002 *Phys. Lett. A* **293** 67–73
[45] Qiao K, Ding Z, Kong J, Chen M, Matthews L S and Hyde T W 2018 arXiv:1810.07173
[46] Nayfeh A H and Mook D T 1979 *Nonlinear Oscillations* (Hoboken, NJ: Wiley) (https://doi.org/10.1002/9783527617586)
[47] Epstein P S 1924 *Phys. Rev.* **23** 710
[48] Chen M, Dropmann M, Zhang B, Matthews L S and Hyde T W 2016 *Phys. Rev.* E **94** 033201
[49] Douglass A, Land V, Qiao K, Matthews L and Hyde T 2016 *J. Plasma Phys.* **82** 615820402
[50] Tomme E B, Law D A, Annaratone B M and Allen J E 2000 *Phys. Rev. Lett.* **85** 2518
[51] Tomme E B, Annaratone B M and Allen J E 2000 *Plasma Sources Sci. Technol.* **9** 87
[52] Prior N J, Mitchell L W and Samarian A A 2003 *J. Phys. D: Appl. Phys.* **36** 1249
[53] Lampe M, Joyce G, Ganguli G and Gavrishchaka V 2000 *Phys. Plasmas* **7** 3851
[54] Konopka U, Morfill G E and Ratke L 2000 *Phys. Rev. Lett.* **84** 891